INTERFACE

royalsocietypublishing.org/journal/rsif

Research

Cite this article: Chandler TGJ, Ferria J, Shorthose O, Allain J-M, Maiolino P, Boudaoud A, Vella D. 2025 Mechanics of pressurized cellular sheets. *J. R. Soc. Interface* **22**: 20240653.
https://doi.org/10.1098/rsif.2024.0653

Received: 19 September 2024
Accepted: 13 December 2024

Subject Category:
Life Sciences–Engineering interface

Subject Areas:
biomechanics

Keywords:
turgor, cellular solids, bryophytes

Authors for correspondence:
Thomas G. J. Chandler
e-mail: tgchandler@wisc.edu
Dominic Vella
e-mail: dominic.vella@maths.ox.ac.uk

Electronic supplementary material is available online at https://doi.org/10.6084/m9.figshare.c.7658831.

THE ROYAL SOCIETY
PUBLISHING

Mechanics of pressurized cellular sheets

Thomas G. J. Chandler[1,2], Jordan Ferria[3], Oliver Shorthose[5], Jean-Marc Allain[4,6], Perla Maiolino[5], Arezki Boudaoud[3] and Dominic Vella[1]

[1]Mathematical Institute, University of Oxford, Woodstock Rd, Oxford OX2 6GG, UK
[2]Department of Mathematics, University of Wisconsin-Madison, Madison, WI 53706, USA
[3]LadHyX, CNRS, Ecole Polytechnique, and [4]LMS, CNRS, Ecole Polytechnique, Institut Polytechnique de Paris, Palaiseau Cedex 91128, France
[5]Department of Engineering Science, University of Oxford, Parks Road, Oxford OX1 3PJ, UK
[6]Institut Nationale de Recherche en Informatique et en Automatique, Palaiseau 91128, France

TGJC, 0000-0001-5351-5399; AB, 0000-0002-2780-4717; DV, 0000-0003-1341-8863

Everyday experience shows that cellular sheets are stiffened by the presence of a pressurized gas: from bicycle inner tubes to bubble wrap, the presence of an internal pressure increases the stiffness of otherwise floppy structures. The same is true of plants, with turgor pressure (due to the presence of water) taking the place of gas pressure; indeed, in the absence of water, many plants wilt. However, the mechanical basis of this stiffening is somewhat opaque: simple attempts to rationalize it suggest that the stiffness should be independent of the pressure, at odds with everyday experience. Here, we study the mechanics of sheets that are a single-cell thick and show how a pressure-dependent bending stiffness may arise. Our model rationalizes observations of turgor-driven shrinkage in plant cells and also suggests that turgor is unlikely to provide significant structural support in many monolayer leaves, such as those found in mosses. However, for such systems, turgor does provide a way to control leaf shape, in accordance with observations of curling upon drying of moss leaves. Guided by our results, we also present a biomimetic actuator that uncurls upon pressurization.

1. Introduction

As well as being vital for the biological function of plants generally, water plays a key role in the mechanics of herbaceous plants in particular. As examples, consider *Mimosa pudica* leaves, which are known to curl due to a change in thickness across the leaf hinge (pulvinus) caused by the motion of water between neighbouring cells [1,2]. Additionally, the movement of water inside bulliform cells can open and close the leaf halves of grasses in the absence of a leaf hinge [3]. Water can also be used to propagate information about deformation over long distances within the plant [4]. Indeed, water is a primary driver of the motion of plants [5].

Perhaps the most obvious manifestation of water (or the lack of it) on plants is wilting under water stress. The everyday experience of plants drooping under their weight when deprived of sufficient water shows that, for many herbaceous plants, turgor must play a significant role in providing the rigidity that allows them to support their own weight. As well as being a consequence of the loss of turgor, wilting may feed back on turgor by reducing the rate of evapotranspiration and water loss [6].

However, not all plants respond to the loss of water in this same way: for example, mosses, resurrection plants and reeds curl up rather than wilting [7–9], while palm leaves may exhibit corrugated folding [10]. The lack of observations of wilting in mosses and other bryophytes might be due to the small size (and, hence, negligible effect of gravity) of the leaves, but nevertheless raises the question of what is the most important mechanical effect of turgor in such systems?

The leaves of mosses have a number of unusual features compared with the leaves of larger species. Firstly, mosses are bryophytes and thus lack true vasculature; as well as having significance for the transport of water throughout the leaf, this lack of vasculature means that, except for the midrib of the leaf, there are no specific structures that stiffen it. An important second difference is that the leaves of mosses are often a single cell thick [11]. It is thus not clear *a priori* how such leaves resist bending under their own weight, for example.

It is natural to seek an understanding of the source of the rigidity of a monolayer leaf by seeking an analogy with highly pressurized membrane shells (such as a cylindrical balloon) [12,13]. As for an elastic beam, the resistance to bending of such a structure comes from the asymmetry between the in-plane stress across the cross-section of the shell. Counter-intuitively, however, this resistance to bending is independent of the internal pressure, at least for small bending deflections [12,13]—pressure dependence enters only once the shell wrinkles or is subject to the Brazier instability [13]. (We give a brief explanation of this surprising result in appendix A). This expectation that pneumatic pressure does not ordinarily supply significant additional mechanical stiffness to an object was confirmed by experiments [14]. Nevertheless, there has been considerable interest in the use of pneumatic pressure (analogous to turgor) to control the shape of artificial structures: by designing the channel structure carefully, pneumatically controlled structures (or 'baromorphs') can be made to have an (almost) arbitrary shape in three dimensions when actuated by pneumatic pressure [15,16], while inflatable structures offer a readily transportable alternative to traditional structures [17]. Taking more direct inspiration from biology, other solutions have used osmotically driven flow as an actuator [18,19], or indeed plant leaves themselves [9]. These structures often consist of inflated 'tubes' connected by a thin flexible strip. These strips provide a small resistance against bending that is also independent of the tube inflation pressure [15]. Connecting the tubes directly, however, would yield a greater bending resistance dependent on the inflation pressure; this is demonstrated in figure 1a,b using a chain of inflated 'air pillows'. These connected structures are also a better reflection of the cellular structure of moss leaves, see figure 1c. They are, thus, the main subject of interest in this paper.

This study is motivated by the twin questions of whether turgor pressure provides significant stiffening against the effects of gravity for mosses and, further, whether the loss of turgor plays a role in the curling of desiccated leaves that is observed [6,7,20–22]. To address these questions, we develop generic two-dimensional models of a single layer of pressurized cells and study their mechanical properties as well as the change of shape that occurs with changes in pressure. Since three-dimensional deformation changes the Gaussian curvature of a thin object, they are energetically expensive in comparison with two-dimensional deformations [23]; as such, we anticipate that considering a two-dimensional structure will provide a useful starting point to address these questions. Moreover, our model goes beyond the geometrical models of [16] to incorporate the mechanics of the cell wall in a simple way.

2. Effects of pressure in symmetric cells

We begin by considering the simplest model with a periodically repeated two-dimensional cell that is up–down symmetric. We shall consider the cell deformation that is induced by pressurization alone, and also study the response of a pressurized element to an imposed bending deformation. (Throughout this paper, we shall assume left–right symmetry). We consider the effect of pressure, which results from water transport in plants, but do not consider other mechanical effects of the water; in particular the bulk modulus of water is neglected.

2.1. Model set-up

We model the two-dimensional cell as being made up of four distinct beams; these represent two surface walls (of thickness h, Young's modulus E and relaxed length L), which are clamped at an exterior angle Θ to the ends of two lateral walls, see figure 1d. (Initially, we assume the two surface walls have the same properties, but shall revisit this assumption in due course). The two lateral walls have the same thickness and Young's modulus, but have a relaxed length $\mathcal{A}L$, so that the cell 'aspect ratio' is $\mathcal{A}$; the deformed length is t. (Note that, because of the two-dimensional nature of the problem, the presence of natural curvature is not important in what follows).

The cell interior is pressurized to a constant pressure p and subject to a moment μ, which stretches and rotates the lateral walls and deforms the surface walls. For zero applied moment, $\mu = 0$, we expect the lateral walls to be vertical thanks to the up–down symmetry of the system. With non-zero μ, the lateral walls are held flat by the adjacent cells, but rotate to an angle ϕ to the vertical at an average horizontal distance w away from each other, see figure 1d. Here, the horizontal cell width w, lateral wall length t and angle ϕ are set by requiring that each cell be in equilibrium.

For the cell to be in equilibrium with the internal pressure, p, and bending moment, μ, the lateral and surface walls must exert a force on each other, which we denote $(T_\pm, N_\pm)$ for the top ('+') and bottom ('−') walls. A force and torque balance yields expressions for $T_\pm$ and $N_\pm$—see electronic supplementary material, equation (S1) of [24]. With these expressions, we turn to consider the deformation of each wall individually.

2.1.1. Deformation of the lateral walls

By construction, the lateral walls remain flat for all interior pressures and only deform longitudinally due to a constant tension (thickness-integrated stress), $\widetilde{T} := \pm N_\pm \cos\phi \mp T_\pm \sin\phi$. Assuming the lateral walls deform according to linear elasticity, the

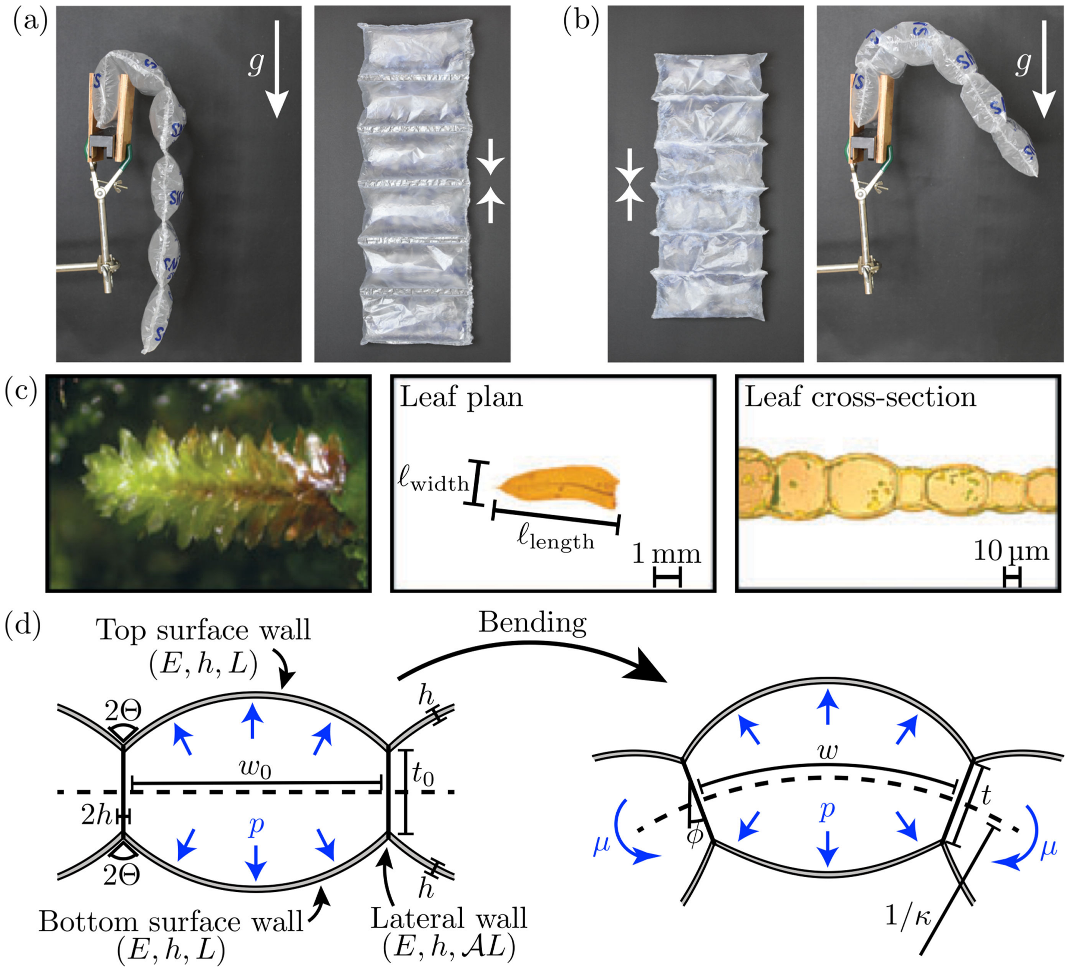

Figure 1. (*a*,*b*) Gravity-driven deflections of a chain of inflated plastic 'air pillows' clamped vertically at one end. In (*a*), the air pillows are connected by a thin flexible strip; while in (*b*), they have been glued directly together (as indicated by the white arrows). (*c*) Photographs of the canopy, leaf and mid-leaf cross-section of the ground-dwelling moss *Distichophyllum freycinettii*. (Figure 1c was originally published in Waite & Sack [20] (2010; © The Authors) and is reproduced under license with permission of John Wiley and Sons, all rights reserved). (*d*) Sketch of the symmetric pressurized cell model considered in §2. The monolayer cell sheet is bent by the application of a bending moment, μ. The structure's resistance to bending is described by the effective bending modulus of the cell, B_{eff}, which we determine in terms of the cell geometry, the Young's modulus of the cell walls, E, and the internal pressure, p.

deformed length, t, satisfies Hooke's law, $\tilde{T} = Y[t/(\mathcal{A}L) - 1]$ where $Y := Eh$ is the two-dimensional Young's modulus of the cell walls. Combining this with the expressions for $N_\pm$ and $T_\pm$ referred to above, we find [25] that t satisfies the quadratic equation

$$\frac{t}{\mathcal{A}L} = 1 + \frac{1}{Y}\left(\frac{pw}{2\cos\phi} - \frac{\mu\tan\phi}{t}\right). \tag{2.1}$$

To determine the lateral wall angle ϕ and cell width w requires us to consider the deformation of the surface walls.

2.1.2. Deformation of the surface walls

We are particularly interested in turgid cells, which correspond to large interior pressures (in a sense to be defined later). This means we cannot, in general, assume the surface walls deform with small slopes. Instead, we model wall deflections using the Kirchhoff beam equations [26,27], which account for large (non-linear) slopes, while still assuming infinitesimal midline strains.

For a Kirchhoff beam, one must distinguish between the reference (stress-free) configuration, with arc-length parameter $0 \le S \le L$, and the deformed configuration, with arc-length parameter s. To simplify the following formulation, we work only in the reference coordinate, S, and present the formulation for the top and bottom walls simultaneously. This formulation follows that by Pandey *et al.* [28].

The deformation of the top ('+') and bottom ('−') walls are measured by the axial stretches $\alpha_\pm(S) := \mathrm{d}s_\pm/\mathrm{d}S$ and the wall positions $(x_\pm, z_\pm)$, which are given by the geometric conditions

$$\frac{\mathrm{d}x_\pm}{\mathrm{d}S} = \alpha_\pm \cos\theta_\pm \quad \text{and} \quad \frac{\mathrm{d}z_\pm}{\mathrm{d}S} = \alpha_\pm \sin\theta_\pm, \tag{2.2a,b}$$

where $\theta_\pm(S)$ are the angles of the wall midlines with respect to the horizontal.

Assuming the resultant moment of each wall is linearly related to the change in curvature, the intrinsic equation of the surface walls, $\theta_\pm(S)$, satisfies the Kirchhoff rod equation [27] modified to incorporate an internal pressure [29], which reads

$$\frac{B}{\alpha_\pm}\frac{\mathrm{d}^2\theta_\pm}{\mathrm{d}S^2} = T_\pm\sin\theta_\pm - N_\pm\cos\theta_\pm \pm p(x_\pm\cos\theta_\pm + z_\pm\sin\theta_\pm), \tag{2.3}$$

for $0 \leq S \leq L$, where $B := Eh^3/12$ is the bending modulus of the surface walls. Similarly, assuming the resultant tension is given by Hooke's law (linear elasticity) then the axial stretch, $\alpha_\pm(S)$, is given by

$$Y(\alpha_\pm - 1) = T_\pm\cos\theta_\pm + N_\pm\sin\theta_\pm \pm p(z\theta_\pm - x_\pm\sin\theta_\pm)\,. \tag{2.4}$$

Note that the limit $Y \to \infty$ corresponds to an inextensible beam, for which $\alpha_\pm(S) \equiv 1$. In this limit, (2.3) recovers the equation for an *elastica* subject to a pressure p [26,29]. (Detailed derivations of (2.3) and (2.4) can be found in §I.A.2 of [25]).

2.1.3. Boundary conditions

It is not clear what mechanics should be imposed at the junction between the lateral and surface walls to model the complex structure found in e.g. plant cells. For simplicity and versatility, we concentrate on clamped boundary conditions with an imposed exterior angle $0 \leq \Theta \leq \pi/2$, which reflects the values seen in nature (see figure 1*c*, for example) [20,30]. We, therefore, have the boundary conditions

$$x_\pm(0) = 0, \quad z_\pm(0) = 0, \quad x_\pm(L/2) = \frac{w}{2} \pm \frac{t}{2}\sin\phi, \tag{2.5a–c}$$

$$\theta_\pm(0) = \pm\left(\frac{\pi}{2} - \Theta\right) + \phi, \quad \theta_\pm(L/2) = 0, \tag{2.5d,e}$$

where the ± refers to the top and bottom surface walls, respectively. Here, (2.5a) are conditions based on the geometry of the cell, (2.5d) is a clamping condition, and (2.5e) comes from the symmetry of the cell.

The two extra boundary conditions for $x_\pm$, i.e. (2.5c), determine the unknown cell width, w, and lateral wall angle, ϕ. Thus, solving (2.2a,b) and (2.3) subject to (2.5) for both surface walls determines w, ϕ and, hence, t by (2.1).

2.1.4. Non-dimensionalization

To develop an understanding of the general behaviour of our model beyond specific parameter values, we non-dimensionalize the governing system (2.1)–(2.5). In this non-dimensionalization, we use the relaxed length of the surface walls, L, as the reference length. This yields a system of ODEs for the surface wall angles of inclination $\theta_\pm$, axial stretches $\alpha_\pm$, and dimensionless position of a point on the walls $(X_\pm, Z_\pm)$—electronic supplementary material, equations (S9)–(S12) of [25].

The non-dimensionalization just described introduces two dimensionless parameters

$$\mathcal{P} := \frac{pL}{Y} \quad \text{and} \quad \mathcal{B} := \frac{B}{YL^2}, \tag{2.6a,b}$$

which measure the internal pressure compared with the stretching of the surface walls and the relative importance of the walls' bending and stretching moduli (i.e. $B = Eh^3/12$ and $Y = Eh$), respectively. ($\mathcal{B}$ may also be thought of as an inverse von Kármán number [31]). The resulting system is governed by the aspect ratio of the cell, $\mathcal{A}$; the inverse Föppl–von Kármán number, $\mathcal{B}$; the dimensionless pressure, $\mathcal{P}$; and the dimensionless applied bending moment, $\hat{\mu} := \mu/(Y\mathcal{A}L)$. Using typical values for the cell wall size $L \approx 50$ μm and $h \approx 1$ μm [20], internal pressure $p \approx 1$ MPa [32] and Young's modulus $E \approx 500$ MPa [32], we find that $\mathcal{B} \sim 10^{-4}$ and $\mathcal{P} \sim 10^{-1}$. Similarly, we find that $\mathcal{B} \approx 1.2 \times 10^{-5}$ and $\mathcal{P} \approx 0.06$ for the inflated pneumatic devices considered by [16]. We shall thus restrict our study to relatively small pressures, $\mathcal{P} \ll 1$, which ensures small axial strains, as required for our assumption of Hooke's law. Crucially, however, we note that the cell becomes turgid when $\mathcal{P} \gg \mathcal{B}$ (pressure dominates bending), which can still be achieved with $\mathcal{P} \ll 1$ provided $\mathcal{B} \ll 1$. (To help the reader interpret the validity of results as $\mathcal{P} \to 1$ appropriately, we shade plots of our numerical results to indicate the maximum strain within the beams, $\epsilon_{\max} = \max_S |\alpha_\pm - 1|$).

The resulting system is solved numerically for given dimensionless parameters $\hat{\mu}$, $\mathcal{P}$, $\mathcal{A}$ and $\mathcal{B}$ using the BVP solver `bvp4c` in MATLAB. This numerical solution determines the unknown lateral wall angle ϕ, the dimensionless lateral wall length $\hat{t} := t/(\mathcal{A}L)$, and the dimensionless cell width $\hat{w} := w/L$. The beams considered here may, in principle, have two stable states (natural and inverted [33]). However, the inverted state was not observed in our numerics: the beams were assumed to initially be in the (energetically favoured) natural state and no snap-through buckling was observed as the internal pressure and bending moments varied. (Had the initial state been the inverted state, snap-through to the natural state may well have occurred). To understand the behaviour of this system, we begin by considering the pressurized structure without any additional forcing, i.e. $\hat{\mu} = 0$.

2.2. The pressurized configuration

With no applied moment, $\hat{\mu} = 0$, the cell walls are in equilibrium with the internal pressure. The cell is up–down symmetric and we expect the lateral walls to be vertical, $\phi = 0$, by symmetry. We denote the (*a priori* unknown) dimensionless cell thickness and width with no applied moment using subscript '0', i.e. $\hat{t}_0$ and $\hat{w}_0$.

2.2.1. Pressure increases cellular area

For a flaccid cell with no internal pressure ($\mathcal{P} = 0$), the two surface walls are circular segments attached to a rectangular centre (bounded by the lateral walls). Our numerical solutions (see figure 2a, for example) show that increasing the pressure, $\mathcal{P}$, increases the enclosed area, $\widehat{A}_0$, by bending the surface walls until the cell resembles a circle with two removed segments—corresponding to the two lateral walls—provided that $\mathcal{B} \ll \mathcal{P}$ (i.e. the cell is turgid). (Further details are given in ection I.B of [25], where we also show that the resistance to expansion initially increases with pressure, but ultimately decreases at large pressures. This increase in resistance could explain observations of a non-linear volume–pressure response in plants without material non-linear elasticity, e.g. [34]).

2.2.2. Pressurized cells can shrink laterally

Our numerical results show that, although turgor pressure drives an increase in cell area, it can cause cells to shrink laterally with increasing pressure, see figure 2b. To understand this, apparently counter-intuitive, result, note that for large Θ the flaccid cell resembles an ellipse with horizontal major axis, and the initial increase in area caused by pressure is achieved by pulling the two lateral walls inwards ($\widehat{w}_0$ decreases); for smaller Θ, the flaccid cell resembles an ellipse with vertical major axis, and the area is initially increased by pushing out the two lateral walls ($\widehat{w}_0$ increases), more in accordance with intuition. These two behaviours are separated by a critical inclination angle, $\Theta = \Theta_{\max}$, for which the flaccid cell is circular and the area can only be increased through stretching ($\widehat{w}_0$ is initially constant). Example profiles of the cells in these three cases are plotted in figure 2①–③. The critical angle separating these two behaviours, $\Theta_{\max}$, is found by elementary geometry to satisfy

$$\sin\Theta_{\max} = \mathcal{A}(\pi/2 - \Theta_{\max}). \tag{2.7}$$

We also note that the internal pressure affects the response of the monolayer to stretching and compression. Quantitative measures for the resistance to increasing pressure (i.e. the effective bulk modulus, K_{2D}) and to axial stretching at fixed pressure (i.e. the effective stretching modulus, Y_{eff}) can be found in section II.A–B of [25]. We now turn to consider the effect of a non-zero applied torque, $\widehat{\mu} \neq 0$.

2.3. Response to bending: an effective bending modulus

When a bending moment, $\widehat{\mu}$, is applied about the midline, the pressurized configuration is expected to bend, so that its midline adopts some curvature, κ—see figure 1d. This induced curvature deforms the surface walls, breaking the up–down symmetry, and so ϕ is non-zero with $\kappa = 2\sin\phi/w$ (by elementary geometry). The symmetry under $\widehat{\mu} \to -\widehat{\mu}$ suggests that the induced rotation $\phi \propto \widehat{\mu}$, at least for sufficiently small moments ($\widehat{\mu} \ll 1$). The analogy with the linear relationship between moment and curvature of a naturally flat beam leads us to introduce an *effective bending modulus*, $B_{\text{eff}} := \lim_{\phi\to 0} \mu/\kappa = \lim_{\phi\to 0} \mu w/(2\phi)$.

For $\phi \ll 1$, our system shows that indeed $\phi \propto \widehat{\mu}$ and the effective bending stiffness, B_{eff}, is well-defined. To non-dimensionalize B_{eff}, we use the stiffness of a flaccid cell ($\mathcal{P} = 0$) with $\Theta = \pi/2$[1]. Bending this configuration induces a strain $\varepsilon = \pm\mathcal{A}L\kappa/2$ in the top ('+') and bottom ('−') walls, hence the effective bending modulus is $B^0_{\text{eff}} := Y(\mathcal{A}L)^2/2$, and we introduce $\widehat{B}_{\text{eff}} := B_{\text{eff}}/B^0_{\text{eff}} \sim \widehat{w}_0\widehat{\mu}/(\mathcal{A}\phi)$.

In general, $\widehat{B}_{\text{eff}}$ must be determined numerically; however, analytical progress can be made in the asymptotic limits of small and large pressures (i.e. turgid and flaccid cells). Below, we present the final asymptotic forms of $\widehat{B}_{\text{eff}}$; derivations can be found in section II.C of [25].

2.3.1. Flaccid cells

For a vanishing internal pressure, $\mathcal{P} = 0$, we find that $\widehat{B}_{\text{eff}}$ is determined by the geometry of the cell, i.e. $\widehat{B}_{\text{eff}} \sim \widehat{B}^0_{\text{eff}}(\Theta, \mathcal{A}, \mathcal{B})$ for $\mathcal{P} \ll 1$ where $\widehat{B}^0_{\text{eff}}$ is (S31) of [25]. Here, the dependence on $\mathcal{B} \ll 1$ determines whether the surface walls respond by bending or stretching and $\mathcal{A}$ controls the aspect ratio of the cell. For $\Theta = \pi/2$, $\widehat{B}^0_{\text{eff}} = 1$ (by choice of reference value), while for $\Theta = 0$, $\widehat{B}^0_{\text{eff}} = 4\pi(\pi^2 + 4/\mathcal{A})\mathcal{B}/(\pi^4\mathcal{B} + \pi^2 - 8) \ll 1$; this agrees with the observation that $\widehat{B}_{\text{eff}}$ increases with the exterior clamping angle, Θ; see figure 3.

2.3.2. Turgid cells

For a large internal pressure, $\mathcal{P} \gg \mathcal{B}$, we find that

$$B_{\text{eff}} \sim \frac{2R_0^3 t_0 w_0}{2R_0 w_0 - L t_0}\, p, \tag{2.8}$$

where $R_0 := (w_0^2 + t_0^2)^{1/2}/2$, w_0, and t_0 are the pressurized cell's radius, width and thickness, respectively, which also depend on the pressure. For $\mathcal{B} \ll \mathcal{P} \ll 1$, (2.8) increases linearly with the pressure. For moderate pressures, $\mathcal{P} \sim 1$, we see a superlinear effect, although at such values the straining of the beams is important, and so the assumption of small strains may no longer

---

[1] A more natural choice of reference state might be the flaccid cell ($\mathcal{P} = 0$) with the relevant clamping angle, Θ. Our choice leads to a solution independent of Θ at large pressures ($\mathcal{P} \gg \mathcal{B}$), but comes with the caveat that the effects of Θ dominate at small pressures.

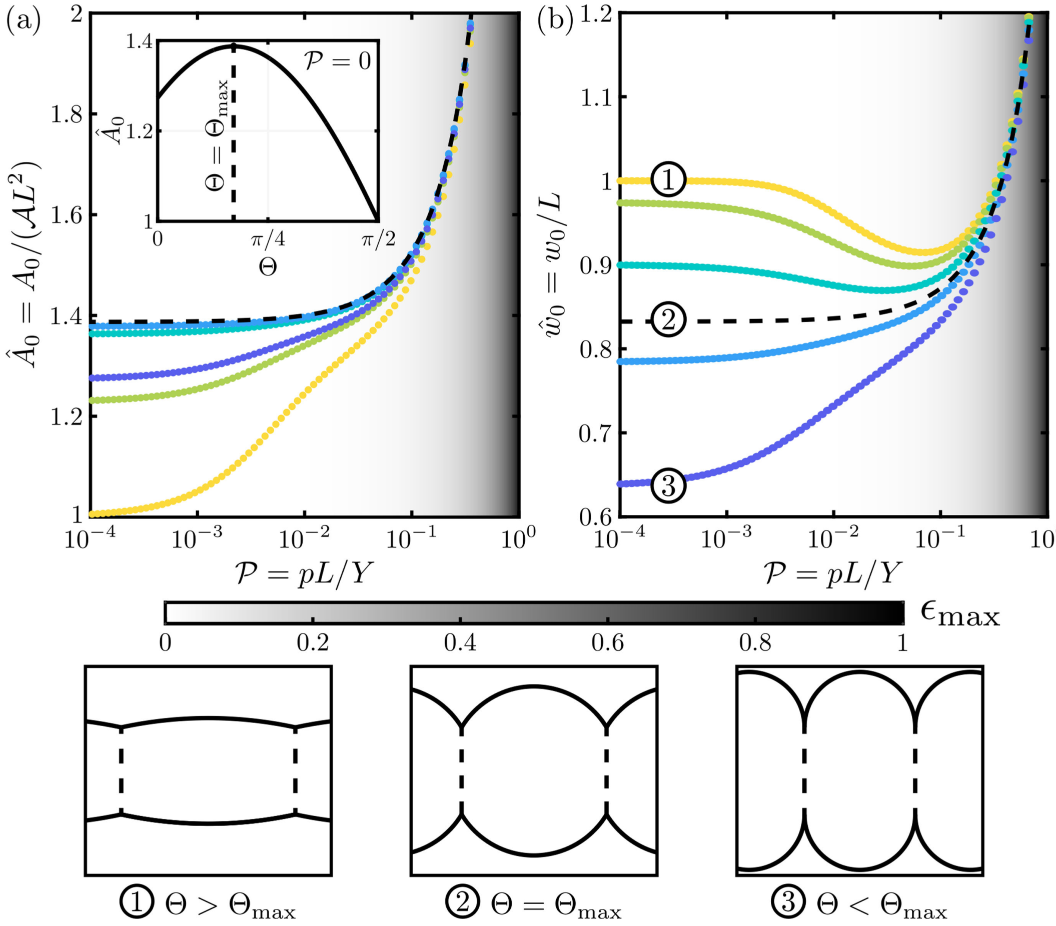

Figure 2. Plots of (*a*) the enclosed area of the cell, $\widehat{A}_0$, and (*b*) the width of the cell, $\widehat{w}_0$, as a function of pressure, $\mathcal{P}$. These plots were numerically determined by solving the Kirchhoff equations with parameters $\mathcal{A} = 1/2$, $\mathcal{B} = 10^{-4}$ and $\Theta = \pi/2, 3\pi/8, \pi/4, \pi/8$ and 0 (yellow to blue dots). The greyscale background corresponds to the maximum strain in the top and bottom beams, $\epsilon_{\max} = \max_S |\alpha_\pm - 1|$, as delineated by the colourbar below these plots. In the inset of (*a*), the area of the flaccid cell (i.e. $\widehat{A}_0$ at $\mathcal{P} = 0$) is plotted as a function of the clamping angle, Θ; this is maximized at $\Theta = \Theta_{\max} \approx 0.54$, for $\mathcal{A} = 1/2$. In the main figures, the solution for $\Theta = \Theta_{\max}$ is plotted as a black dashed curve. In this critical case, the cell is circular in shape, which qualitatively separates the different behaviours: for $\Theta > \Theta_{\max}$, the cell resembles a horizontal ellipse and an increase in pressure initially decreases the cell width, $\widehat{w}_0$; while for $\Theta < \Theta_{\max}$, the cell resembles a vertical ellipse and an increase in pressure initially increases the cell width, $\widehat{w}_0$. These regimes are delineated by ①–③. Note that all the curves (areas and widths) converge when the dimensionless pressure becomes close to one.

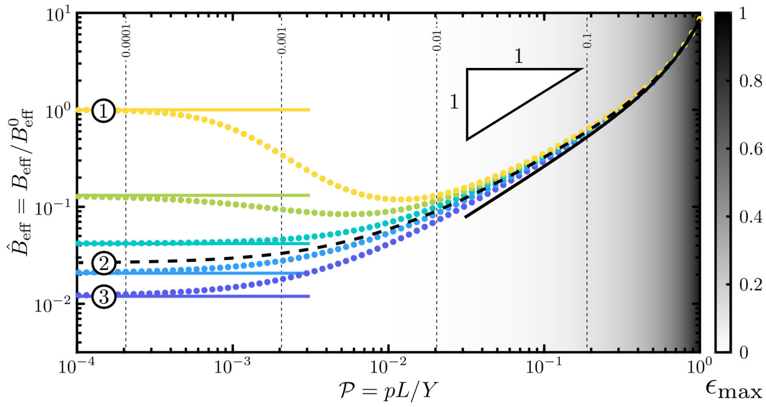

Figure 3. Plot of the effective bending modulus, $\widehat{B}_{\rm eff}$, as a function of the internal pressure, $\mathcal{P}$, for the configuration parameters $\mathcal{A} = 1/2$, $\mathcal{B} = 10^{-4}$ and $\Theta = \pi/2$, $3\pi/8$, $\pi/4$, $\pi/8$ and 0 (yellow to blue). The effective moduli found by numerically solving the Kirchhoff equations are plotted as coloured dots, while asymptotic results are plotted as solid curves: $\widehat{B}_{\rm eff} \sim \widehat{B}^0_{\rm eff}$, valid for small pressures, is shown with the corresponding colour, and (2.8), valid for large pressures, is shown in black. The black dashed curve is the numerical solution with maximum encapsulated area, $\Theta = \Theta_{\max} \approx 0.54$. The greyscale background corresponds to the maximum strain in the top and bottom beams, $\epsilon_{\max} = \max_S |\alpha_\pm - 1|$, as delineated by the colourbar; the contour lines of $\epsilon_{\max} = 10^{-4}$, 10^{-3}, 10^{-2} and 10^{-1} are shown as vertical dashed lines. ①–③ correspond to the three regimes sketched in figure 2. Although $\widehat{B}_{\rm eff}$ may initially decrease with $\mathcal{P}$ (i.e. for large values of Θ), it ultimately increases with $\mathcal{P}$. Note that all the curves (bending stiffnesses) converge when the dimensionless pressure becomes close to one.

be valid (hence the shading in figure 3). An angular stiffness that is linear in the pressure has previously been found for turgid pressurized cells [16]. However, the effects of wall stretching, which gives rise to the observed superlinear response, has not, to our knowledge, been appreciated previously.

2.3.3. Moderate internal pressures

In figure 3, the numerically determined $\hat{B}_{\text{eff}}$ is plotted as a function of $\mathcal{P}$ for $\mathcal{A} = 1/2$, $\mathcal{B} = 10^{-4}$ and various Θ. Also plotted are the asymptotic results at small pressures, i.e. $\hat{B}_{\text{eff}} \sim \hat{B}^0_{\text{eff}}$, and large pressures, i.e. (2.8). As well as showing that the expected asymptotic behaviour is recovered by these numerics, figure 3 shows that $\hat{B}_{\text{eff}}$ may initially decrease with pressure, $\mathcal{P}$, if the exterior clamping angle, Θ, is sufficiently large, but ultimately it increases with $\mathcal{P}$ according to (2.8). Altering the configuration parameters, $\mathcal{A}$ and $\mathcal{B}$, changes the results presented here quantitatively, but not qualitatively.

3. Pressure-dependent morphing in asymmetric cells

Many leaves are observed to curve when they dry [7,8,10]. One benefit of curving a water-stressed leaf is to decrease the rate of evaporation, while the benefit of being flat when not water-stressed is to increase the area available to intercept sunlight [10]. However, an up–down symmetric structure will not change its moment-free curvature, regardless of the turgor pressure. To understand the turgor-driven curvature of leaves, therefore, requires an asymmetry, either mechanical or geometrical, to be introduced at the cellular level. In this section, we consider the effect of different asymmetries on the variation of tissue curvature with pressure.

3.1. Equilibrium equations of the asymmetric cell

To introduce an asymmetry in our cell model, we allow the surface walls to differ in one or more of the following properties: relaxed length L, thickness h, Young's modulus E and/or clamping angle Θ. We, therefore, replace $\{E, h, L, \Theta\}$ with $\{E_\pm, h_\pm, L_\pm, \Theta_\pm\}$ for the top ('+') and bottom ('−') surface walls. Other than this notational change, the mathematical formulation for such an asymmetric cell is identical to the symmetric case considered in §2, but with $\mu = 0$ since we neglect any applied bending moment. For clarity, here, we also relabel the Young's modulus, thickness and relaxed length of the lateral walls as E_{L}, h_{L} and L_{L}, respectively. This set-up is sketched in figure 4.

Using the relaxed lengths of the surface walls as the reference lengths, the surface walls' slopes $\theta_\pm$, axial stretches $\alpha_\pm$ and dimensionless position of a point on the surface walls $(X_\pm, Z_\pm)$ satisfy a system of ODEs, electronic supplementary material, equations (S9)–(S13) of [25]. These equations are governed by the same dimensionless parameters that were introduced for the symmetric case (§2.1), albeit with subscript distinguishing between the top ('+') and bottom ('−') surface walls, i.e. $\mathcal{P}_\pm$, $\mathcal{A}_\pm$, $\mathcal{B}_\pm$, $\Theta_\pm$ and $\hat{w}_\pm$. Additionally, we introduce a new parameter,

$$\mathcal{Y}_\pm := \frac{E_{\text{L}} h_{\text{L}}}{E_\pm h_\pm}, \tag{3.1}$$

which is the ratio of the stretching moduli for the top and bottom walls compared with the lateral walls. (Note that $\mathcal{Y}_\pm = 1$ for the homogeneous symmetric cell considered in §2.1).

By introducing the parameter ratios,

$$\mathcal{R}_E := E_-/E_+, \quad \mathcal{R}_h := h_-/h_+, \quad R_L := L_-/L_+, \quad \mathcal{R}_\Theta := \Theta_-/\Theta_+, \tag{3.2a–d}$$

the parameters for the bottom wall can be written in terms of those for the top wall. The difference of the ratios in (3.2) from unity measures the asymmetry of the cell. Overall, given values for the top surface wall parameters ($\mathcal{P}_+$, $\mathcal{A}_+$, $\mathcal{B}_+$, $\mathcal{Y}_+$ and Θ_+) and the asymmetric ratios ($\mathcal{R}_E$, $\mathcal{R}_L$, $\mathcal{R}_h$ and $\mathcal{R}_\Theta$), the system for the top and bottom walls can be solved to determine the cell width $\hat{w}_+ \equiv \mathcal{R}_L \hat{w}_-$, cell thickness $\hat{t}$ and lateral wall angle ϕ. We now turn to consider a macroscopic measure of the asymmetric cells, namely the effective curvature.

3.2. Effective curvature

At the scale of a whole leaf, individual cells cannot be identified, instead the asymmetry in e.g. plant tissue is observed as an intrinsic curvature. In the case of the asymmetric cell model introduced in §3.1, this *effective curvature* is the curvature of the cell midline which, from simple geometrical arguments, can be written as

$$\varkappa_{\text{eff}} := 2\sin\phi/w, \tag{3.3}$$

where we associate a positive curvature with a positive angle ϕ for the left lateral wall (i.e. the cell curves downwards, figure 4). As we show below, the scale of $\varkappa_{\text{eff}}$ and how it varies with $\mathcal{P}$ is dependent on the type and magnitude of asymmetry chosen; thus, there is no obvious choice of a dimensionless scale for $\varkappa_{\text{eff}}$. Instead, we choose L_{L} (the relaxed length of the lateral walls) as a reference length to aid the comparison between the different asymmetries, i.e. we define $\hat{\varkappa}_{\text{eff}} := L_{\text{L}} \varkappa_{\text{eff}} = 2\mathcal{A}_\pm \sin\phi/\hat{w}_\pm$.

In figure 5, we plot the curvature of the cell, $\hat{\varkappa}_{\text{eff}}$, obtained numerically, as a function of the internal pressure with one asymmetry introduced at a time. Also plotted are asymptotic predictions, which hold for small and large pressures—details of these can be found in section II.D of [25]. It is apparent that the different types of asymmetry induce variations of curvature with pressure that are qualitatively different. Below, we explain the results for each type of asymmetry.

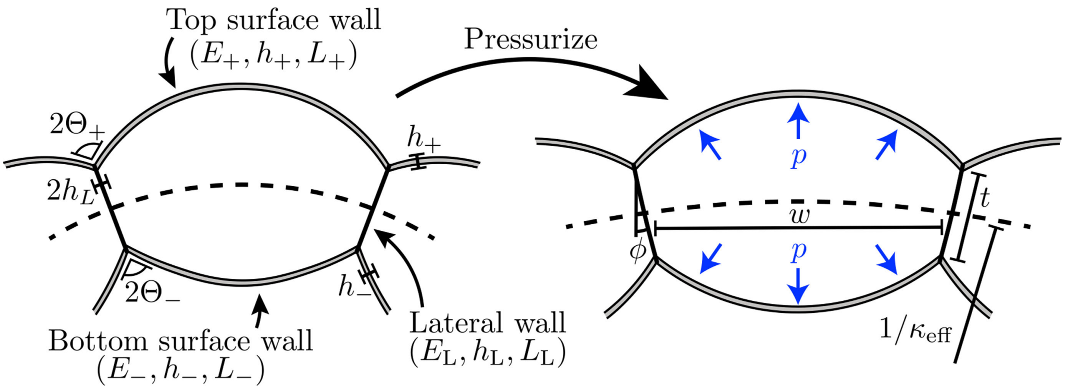

Figure 4. Sketch of the asymmetric pressurized cell model considered in this section. The top and bottom surface walls have differing values of Young's moduli $E_\pm$, thicknesses $h_\pm$, relaxed lengths $L_\pm$ and/or clamping angles $\Theta_\pm$. These asymmetries induce an effective curvature, κ_eff, which varies with the internal pressure, p.

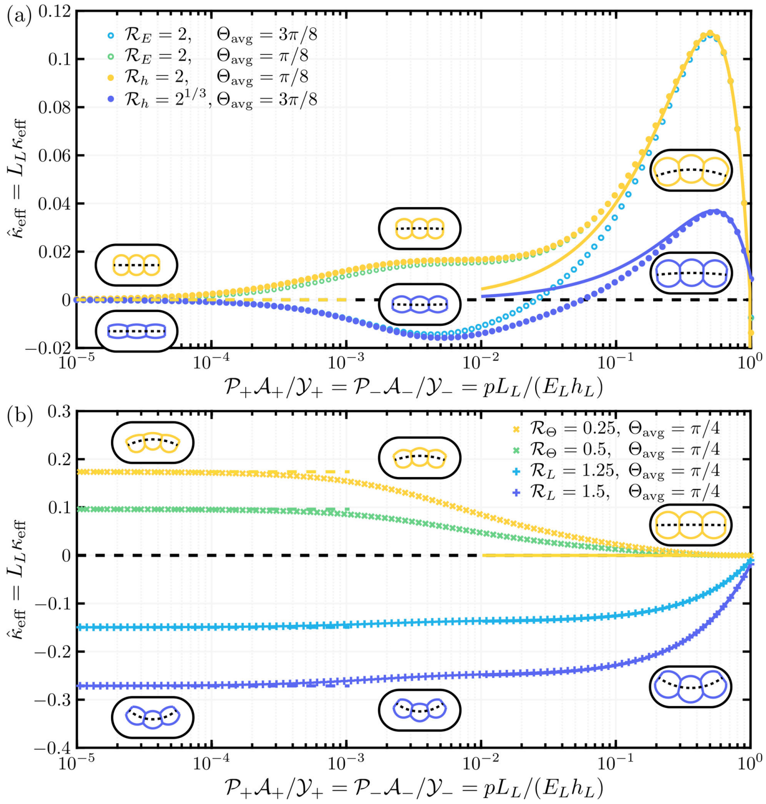

Figure 5. Plots of the numerically determined effective cell curvature, $\hat{\kappa}_\mathrm{eff}$, as a function of the internal pressure for an asymmetry in either the Young's modulus ($\circ$ in panel (*a*)), thickness ($\bullet$ in panel (*a*)), relaxed length ($+$ in panel (*b*)), or clamping angle ($\times$ in panel (*b*)) of the surface walls, where the corresponding values of $\mathcal{R}_E$, $\mathcal{R}_h$, $\mathcal{R}_L$ or $\mathcal{R}_\Theta$ (asymmetries in the Young's modulus, thickness, length and clamping angle, respectively) are given in the keys. (Note that the ratio values, and hence the sign of curvature, are chosen for presentation purposes only). The parameters are chosen such that their averages recover those used in figure 3, that is $(1/\mathcal{Y}_+ + 1/\mathcal{Y}_-)/2 = 1$, $(1/\mathcal{A}_+ + 1/\mathcal{A}_-)/2 = 1/2$, $(\mathcal{B}_+ + \mathcal{B}_-)/2 = 10^{-4}$ and $(\Theta_+ + \Theta_-)/2 = \Theta_\mathrm{avg}$, where in (*a*), $\Theta_\mathrm{avg} = 3\pi/8$ (blues) and $\pi/8$ (yellow and green), and in (*b*), $\Theta_\mathrm{avg} = \pi/4$. Also plotted are the asymptotic results for small pressures (as dashed lines) and large pressures (as solid curves), as derived in ection II.D of [25], and the cell profiles for the asymmetry with the corresponding colour at $\mathcal{P} = 0$, $10^{-5/2}$ and $10^{-1/2}$ (left to right).

3.2.1. Asymmetry in the Young's modulus ($\mathcal{R}_E \neq 1$)

At small internal pressures, the surface walls are unstrained since their ends are free to move horizontally; thus, an asymmetry in the Young's modulus of the surface walls does not induce a curvature at small pressures. As the pressure increases, however, the walls deform in response to the additional loading. Initially, the cell curves towards or away from the more compliant wall, depending on whether decreasing or increasing the width of the cell increases its area—i.e. $\Theta < \Theta_\mathrm{max}$ or $\Theta > \Theta_\mathrm{max}$, respectively, with Θ_max given by (2.7). (In the case of figure 5a, $\mathcal{R}_E = 2 > 1$, so the top surface wall is more compliant; thus, for $\Theta = 3\pi/8 > \Theta_\mathrm{max} \approx 0.54$, the cell initially bends upwards and $\hat{\kappa}_\mathrm{eff}$ is negative, while for $\Theta = \pi/8 < \Theta_\mathrm{max} \approx 0.54$, it bends downwards and $\hat{\kappa}_\mathrm{eff}$ is positive). As the pressure increases further, i.e. for $\mathcal{P}_\pm \gg \mathcal{B}_\pm$, the cell approaches a circular arc, thus the walls do not bend any more and, instead, stretch under an increase in pressure. Again, the more compliant wall deforms at lower pressures; this increases its length and bends the cell away from it, regardless of the clamping angle, Θ. (In figure 5a, the cell curves downwards at large pressures for both $\Theta = 3\pi/8$ and $\pi/8$). Finally, for $\mathcal{P}_\pm \sim 1$, the pressure is sufficiently large that both walls are able to stretch freely, resulting in the cell flattening.

3.2.2. Asymmetry in the surface wall thicknesses ($\mathcal{R}_h \neq 1$)

An asymmetry in the surface wall thickness is analogous to the asymmetry in the Young's modulus, with the induced curvature depending on the pressure in a qualitatively identical way. In fact, since the walls only bend at small pressures and the bending modulus $B \propto Eh^3$, taking $\mathcal{R}_E = \mathcal{R}$ and $\mathcal{R}_h = 1$ is the same as taking $\mathcal{R}_E = 1$ and $\mathcal{R}_h = \mathcal{R}^{1/3}$ at small pressures. Conversely, for large pressures, it is the stretching modulus $Y \propto Eh$ that matters, so taking $\mathcal{R}_E = \mathcal{R}$ and $\mathcal{R}_h = 1$ is the same as taking $\mathcal{R}_E = 1$ and $\mathcal{R}_h = \mathcal{R}$ at large pressures. This correspondence is shown in figure 5a for $\mathcal{R} = 2$.

3.2.3. Asymmetry in the surface wall lengths ($\mathcal{R}_L \neq 1$)

If one of the surface walls is naturally longer than the other, then the cell must be curved in its natural state. (In the case of figure 5b, $\mathcal{R}_L > 1$, so the bottom surface wall is longer than the top and the cell is curved upwards—$\widehat{\kappa}_{\text{eff}}$ is negative). As the pressure increases, the curvature smoothly transitions from the results for a flaccid cell (governed by geometry) to those of a turgid cell, see sectionII.C of [25]. At very large pressures, $\mathcal{P}_\pm \gtrsim 1$, the walls are free to stretch and so the cell grows, resulting in a smaller effective curvature.

3.2.4. Asymmetry in the clamping angles ($\mathcal{R}_\Theta \neq 1$)

For small internal pressures, an asymmetry in the clamping angles causes the cell to be curved away from the shallower-angled surface wall—i.e. the larger value between Θ_+ and Θ_-. (In figure 5b, $\mathcal{R}_\Theta < 1$ so that $\Theta_- < \Theta_+$ and, hence, the cell is curved downwards with a positive $\widehat{\kappa}_{\text{eff}}$). This behaviour is determined purely by elementary geometry. As the pressure increases, however, the importance of the clamped boundary decreases; in particular, for $\mathcal{P}_\pm \gg \mathcal{B}_\pm$ the clamping angles are irrelevant except in boundary layers of width $\mathcal{O}(\mathcal{B}_\pm/\mathcal{P}_\pm)$ close to the ends of the surface walls. Outside these boundary layers, the cell is effectively symmetric with zero curvature. Unlike the other asymmetries, this trend towards zero-curvature can occur at small axial strains ($\mathcal{P}_\pm \ll 1$), where the assumption of linear elasticity still holds, see figure 5b.

Overall, a geometrical asymmetry (e.g. $\mathcal{R}_L \neq 1$ or $\mathcal{R}_\Theta \neq 1$) tends to lead to a curvature when flaccid, which vanishes as the internal pressure increases; while a mechanical asymmetry (e.g. $\mathcal{R}_E \neq 1$ or $\mathcal{R}_h \neq 1$) tends to lead to no curvature when flaccid and a high curvature when turgid. In reality, multiple asymmetric properties might be combined in such a way as to have conflicting effects, and so the curvature, $\widehat{\kappa}_{\text{eff}}$, might vary with the pressure differently to that discussed. However, the asymptotic results for small and large pressures [25], still hold true and can be used as a first step towards understanding how $\widehat{\kappa}_{\text{eff}}$ varies with pressure.

4. Biological implications

In §§2 and 3, we presented the results of detailed model calculations for a monolayer cell sheet subject to an internal pressurization. To understand the effective rigidity of such sheets, we focused on cell sheets that are up–down symmetric (§2); this also allowed us to understand changes in length of the sheet caused by pressurization. Cell sheets with embedded up–down asymmetry added the possibility of out-of-plane shape changes (§3). We now turn to several biological systems that share the essential ingredients we have discussed to learn what our modelling tells us about these scenarios.

4.1. Length changes during pressurization

Our model predicted that whether a symmetric cell sheet shrinks or expands upon increasing pressurization depends on the angle at which the beams are clamped. If $\Theta < \Theta_{\max}$, pressure acts to 'iron out' the excess length stored in the arched beams and each cell extends laterally. This behaviour is almost intuitive, and has been reported as part of the explanation for the growth in size of the wings of *Drosophila melanogaster* as they emerge from the pupal stage [35].

However, if $\Theta > \Theta_{\max}$, the opposite behaviour is observed: because the beams are less inclined in this case, their primary response to pressurization is to become more highly curved, which, without stretching, requires the cell to shrink laterally. Though less intuitive, this pressure-induced shrinkage *has* been observed in plant tissue and is highly dependent on the cell geometry and wall anisotropy [30]. Using cellular force microscopy data, Hofhuis *et al*. [30] fitted experimental data for the wall elastic moduli, obtaining $E_\parallel \approx 9000\,\text{MPa}$ and $E_\perp \approx 150\,\text{MPa}$ parallel and perpendicular to the shrinking axes, respectively. With these Young's moduli, their finite element method (FEM) simulations suggest a relative cell length $R_{\text{len}} \approx 0.91$ and volume $R_{\text{vol}} \approx 1.53$ at a turgor pressure $p \approx 0.65\,\text{MPa}$. These are comparable to the values $R_{\text{len}} \approx 0.88$ and $R_{\text{vol}} \approx 1.53$ observed in their experiments. Their results can be directly compared with our two-dimensional model since they assume the cell wall in the third dimension (i.e. perpendicular to the shrinking axis) is soft in comparison with the other dimensions (i.e. parallel to the shrinking axis). Using our model with the same cell parameters (i.e. $h = 0.2\,\mu\text{m}$, $L = 50\,\mu\text{m}$, $\mathcal{A} = 0.4$, $p \approx 0.65\,\text{MPa}$, $E = 9000\,\text{MPa}$ and $\Theta = \pi/2$), we obtain $R_{\text{len}} = \widehat{w}_0 \approx 0.83$ and $R_{\text{vol}} = \widehat{A}_0 \approx 1.53$, which are remarkably similar to the values obtained by their more sophisticated FEM simulations.[2]

Pressure-induced shrinkage has also been used to develop bio-inspired programmable shells [15,16,36] and, in tandem with an element of fixed length, to induce curvature [2]. In particular, the linear increase of curvature with pressure observed experimentally there is consistent with our theoretical work, which suggests a linear increase in size with increasing pressure.

4.2. Size limits for monolayer leaves

The model developed thus far was motivated by the leaves of mosses, which are often a single cell thick, and have no vasculature to stiffen them. Having developed the model of §2, it is natural to use it to understand whether the size of a moss leaf is limited by the ability of turgor pressure to support it against gravity.

4.2.1. Bending under gravity

A horizontally clamped beam (of bending modulus B and linear density ϱ) bends under the influence of its weight when its length, ℓ, is comparable to the elastogravitational length $\ell_{\mathrm{bg}} \coloneqq (B/\varrho g)^{1/3}$, with g the gravitational acceleration [37,38]: if $\ell \gg \ell_{\mathrm{bg}}$, the beam will sag significantly. Such sagging could have two detrimental consequences for a plant leaf: (i) it decreases the incident sunlight that may be captured and (ii) it may lead to large internal strains, which may cause structural failure and damage. Previously, similar constraints for a *heavy elastica* have been used to compute the branch shape with maximum reach [39] and the leaf design that maximizes the light intercepted for photosynthesis [40]. By taking $B = B_{\mathrm{eff}}$ and $\varrho = \rho\ell_{\mathrm{thick}}$, where ρ is the bulk density of the tissue and ℓ_{thick} is the macroscopic thickness, we can compute the typical length scale over which our cellular structure would bend under gravity, i.e. ℓ_{bg}; we then compare ℓ_{bg} with the lateral dimensions of naturally occurring moss leaves, specifically the leaf length and width, ℓ_{width} and ℓ_{length}, as defined in figure 1c.[3]

For small deflections, the change in the horizontal projected area (and, hence, area intercepting sunlight) is $L - x(L) = \int_0^L (1-\cos\theta)\,\mathrm{d}S \propto \int_0^L \theta^2\,\mathrm{d}S$ and, thus, is expected to be quadratic in the relative deflection. The typical relative deflection of the heavy elastica is

$$\mathcal{D} \coloneqq \frac{w(\ell)}{\ell} = \frac{\ell^3}{8\ell_{\mathrm{bg}}^3}, \tag{4.1}$$

where $w(x)$, for $0 \le x \le \ell$, is the profile of the deformed beam (see appendix B and [26]). In conclusion, sufficiently small leaves ($\ell \ll 2\ell_{\mathrm{bg}}$) should not sag significantly under gravity. With the measure of deflection (4.1), we can now test whether turgor pressure is required for rigidifying the width and length of moss leaves against gravity. We shall begin by considering the leaf widths since, unlike the leaf lengths, these do not have the additional support provided by a leaf costa/midrib.

4.2.2. Effect of the width of moss leaves

In figure 6, the leaf widths, ℓ_{width}, of nine different species of single-cell thick moss are plotted against the corresponding elastogravitational lengths, $\ell_{\mathrm{bg}} = [B_{\mathrm{eff}}/(\rho g \ell_{\mathrm{thick}})]^{1/3}$, predicted from our model. Here, we use geometrical parameters for the moss leaves and their cells from [20]. and take the Young's modulus of the cell walls as $E = 100$ MPa (a lower bound on the typically accepted values for plant cells [41]). In figure 6a, the prediction of ℓ_{bg} is calculated assuming that the cells are flaccid ($\mathcal{P} = 0$), while in figure 6b, ℓ_{bg} is calculated assuming a turgor pressure in the range $0.8\ \mathrm{MPa} \le p \le 2.1\ \mathrm{MPa}$ (to reflect the typical values found in moss [32]).

By comparing figure 6a,b, it is apparent that turgor pressure increases the elastogravitational length, ℓ_{bg}. In fact, using the small deflection solution, (4.1) with $\ell = \ell_{\mathrm{width}}/2$, the expected deflection of turgid leaves are all less than 1%, i.e. $[(\ell_{\mathrm{width}}/2)/\ell_{\mathrm{bg}}]^3 = 8\mathcal{D} < 8 \times 10^{-2}$. Nevertheless, even for flaccid cells ($\mathcal{P} = 0$), the expected deflection remains below a few percent.

4.2.3. Effect of the length of moss leaves

The leaf length, ℓ_{length}, of the moss species studied by [20] is typically 3–17 times larger than their width, ℓ_{width}. Multiplying the abscissa of the data plotted in figure 6 by such a large factor would move all data points into the 'dangerous' region where the leaf would be expected to sag under its own weight. Of course, the leaf costa/midrib provides additional longitudinal support along the length of the leaf, and so the simple picture used to understand the likely deformation under gravity of the width of the leaf is not strictly relevant. Nevertheless, the fact that this midrib is significantly thicker than neighbouring tissue (and, hence, does rigidify the leaf) is consistent with the result of our theory that moss leaves are relatively close to the threshold at which gravitational deformation does become significant.

Our results suggest that the widths of leaves are small enough that they do not need rigidifying, but that the lengths are long enough that: (i) turgor does not provide significant additional support beyond that intrinsic to the cell walls and so (ii) the midrib is required to provide structural support against gravitational effects.

---

[2] Note that a slightly pressurized cell was used as a reference state by Hofhuis *et al*. [30] to reflect the observations of actual plant cells. This is in comparison with the truly unpressurized state ($\mathcal{P} = 0$), that we have used here. Using a pressurized cell has the effect of slightly increasing R_{len} and slightly decreasing R_{vol}, but without more details of the slight pressurization used by Hofhuis *et al*. [30] we cannot quantify this effect in our results.

[3] Note that both the length scale over which the beam strains due to bending, $\ell_{\mathrm{bend}} \coloneqq [B_{\mathrm{eff}}/(\rho g \ell_{\mathrm{thick}}^2)]^{1/2}$, and stretches due to gravity, $\ell_{\mathrm{stretch}} \coloneqq Y_{\mathrm{eff}}/(\rho g \ell_{\mathrm{thick}})$, where Y_{eff} is the effective stretching modulus, are typically orders of magnitude larger than the elastogravitational length, ℓ_{bg}, and so are not considered here; nevertheless, further details can be found in appendix B.

(a) Flaccid cell

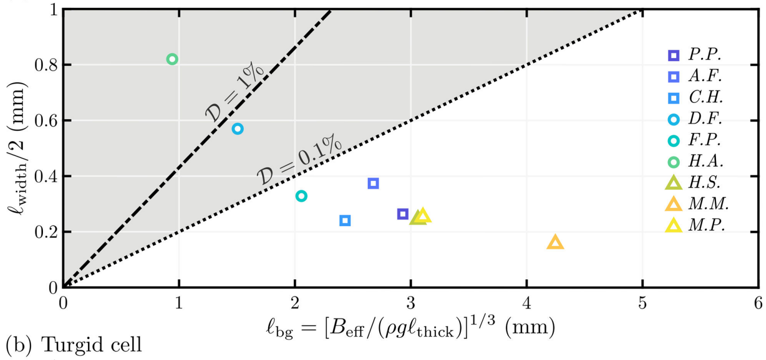

(b) Turgid cell

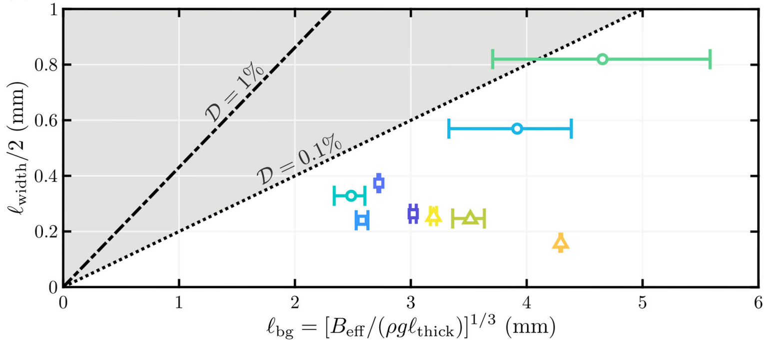

Figure 6. Plot of the extended lamina widths, $\ell_{\mathrm{width}}/2$, against estimated elastogravitational length, $\ell_{\mathrm{bg}} = [B_{\mathrm{eff}}/(\rho g \ell_{\mathrm{thick}})]^{1/3}$, for nine species of single-cell thick moss; here, colour denotes the species (see key), while point shape denotes the type as follows: trunk-dwelling mosses, □, (*Pyrrhobryum pungens*, *Acroporium fuscoflavum*, *Campylopus hawaiicus*); ground-dwelling mosses, ○, (*Distichophyllum freycinetii*, *Fissidens pacificus*, *Hookeria acutifolia*); branch-dwelling mosses, △, (*Holomitrium seticalycinum*, *Macromitrium microstomum*, *Macromitrium piliferum*). Here, we have used the cell width, cell height, cell wall thicknesses, lamina thickness and maximum leaf width reported by [20] for each species to estimate L, $\mathcal{A}L$, h, ℓ_{thick} and ℓ_{width}, respectively. We further assume a density $\rho = 1000$ kg m^{-3}; clamping angle $\Theta = \pi/4$ (based on the cross-sections shown in [20]); Young's moduli $E = 100$ MPa, which is chosen as a lower bound to the typically accepted range in plant cells [41]; and turgor pressures (*a*) $p = 0$ MPa (i.e. a flaccid cell) and (*b*) 0.8 MPa $\leq p \leq$ 2.1 MPa (the typical range found in moss [32], with variation shown by error bars in ℓ_{bg}). The lines $\ell_{\mathrm{width}}/2 = 2\mathcal{D}^{1/3}\ell_{\mathrm{bg}}$ for $\mathcal{D} = 10^{-2}$ (dash-dotted) and $\mathcal{D} = 10^{-3}$ (dotted) correspond to the deflection, $\mathcal{D}$, of an Euler–Bernoulli beam, (4.1); thus, the shaded region corresponds to where appreciable deformation under gravity would be expected.

4.3. Curvature in plant leaves

We have shown that turgor pressure does not provide a significant advantage in terms of rigidifying the leaf against the effect of gravity. We, therefore, turn now to consider how pressure might produce the significant changes in curvature that are seen upon the desiccation of leaves. A hydrated (large turgor pressure) moss leaf is flat to maximize light interception, while a dehydrated (small turgor pressure) moss leaf is tightly curved, which limits further water loss [10,21,22].

To illustrate more concretely this change in curvature, figure 7a,b shows optical coherence tomography images of *Physcomitrium patens* moss leaves when hydrated (turgid) and dehydrated (flaccid). By taking cross-sections of the leaves at fixed points along their length, the effective curvature of the two lamina halves protruding from the midrib were measured by fitting a circle, as demonstrated in figure 7a,b. (Further details of these experiments can be found in appendix C). Figure 7c shows a plot of the hydrated curvature against the dehydrated curvature for a number of leaves and cross-sections. The majority of these points lie below the line $y = x$, suggesting the leaves do indeed curl when they dry. A linear least-squares fit yields a gradient of 0.2169 with a coefficient of determination of $R^2 = 0.2075$ after omitting the three outliers above the $y = x$ line.

We studied the pressure dependence of the curvatures induced by the various asymmetries in figure 5. From this, it appears that an asymmetry in the clamping angles ($\mathcal{R}_\Theta \neq 1$) is closest to qualitatively reproducing the observation that a dehydrated leaf is curved, whilst a hydrated leaf is flat. The green and yellow curves of figure 5b show a curved state at low pressure (dehydrated) that is gradually ironed out by bending as the pressure increases (hydration). Figure 5b shows that an asymmetry in the length of the surface walls also qualitatively recovers this behaviour. However, this is only achieved with $\mathcal{P} \approx 1$ when $\mathcal{R}_L \neq 1$ (see blue curves in figure 5b) because in this case the walls need to stretch (rather than bend) to flatten the leaf.

The results above raise the question of why the curvature control mechanism proposed above is not used by vascular plants. Indeed, resurrection plants seem to curl up by relying on gradients in density of lignin, a hydrophobic component of the cell wall [8]. Most vascular plants wilt when they lose turgor. This difference can be rationalized as follows. In contrast to a curvature induced by dehydration, turgid plant tissue has also been observed to curl; for example, longitudinal strips removed from *Tulipa* stems spontaneously recurve [42]; detached exocarp cells after explosive seed dispersal in *Cardamine hirsuta* curl away from the fruit [30]; and animal epithelial monolayers curl downwards when devoid of a supporting substrate [43]. In all three of these examples it was proposed that the spontaneous curvature was due to an anisotropy between the outer and inner layers of the cellular structure: Niklas & Paolillo Jr [42] suggested that the spontaneous curvature was due to differing mechanical properties across the cell walls (as first suggested by Hofmeister [44]); Hofhuis *et al.* [30] modelled the curling of the detached exocarp as the release of tension inside a structure made of three different materials: an active soft outer layer,

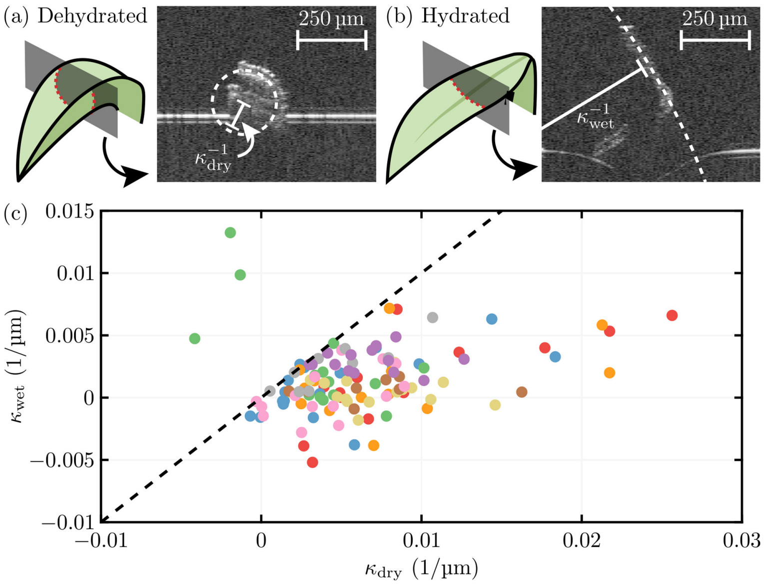

Figure 7. Optical coherence tomography images of a cross-section of a (*a*) dehydrated and (*b*) hydrated *Physcomitrium patens* moss leaf. The two laminar halves protruding from the midrib are approximated by a circle (shown as dashed curves), the radius of which yields the dry and wet signed curvatures, κ_{dry} and κ_{wet}, respectively. (*c*) Plot of κ_{wet} against κ_{dry} for 11 *Physcomitrium patens* leaves at various cross-sections along the leaves' lengths (points with the same colour correspond to measurements at different points along the same leaf). The majority of the points lie below $y = x$ (black dashed line), showing the leaves tend to curl when dehydrated.

a passive middle and a stiff inner layer; and Fouchard *et al*. [43] proposed that the asymmetry of the animal cell sheet was due to an enrichment of Myosin II in the substrate-supported side. Parallels can, thus, be drawn between these observations and the asymmetric Young's modulus (or equivalently thickness) induced curvature, $\mathcal{R}_E \neq 1$ (or $\mathcal{R}_h \neq 1$). Accordingly, our model provides a tool for the qualitative understanding of the curvature of simple cellular structures.

5. Biomimetic control of curvature

In addition to the biological examples considered in §4, the pressure-sensitive curvature of the monolayer cellular sheets considered here may open new possibilities for the design of inflatable structures [16,36,45]. Typically, such structures are flat in the unpressurized state and curve with increasing pressure [36,46,47]; this is usually caused by asymmetries in the thickness or modulus of different sides of the object (see, for example, [46]) and hence gives curvature–pressure evolution of the type shown in figure 5a. However, figure 5b shows that asymmetry in the angles or lengths of the cells may lead to a very different behaviour with the system is initially curved but becoming flat as the pressure increases. As a concrete example, one can imagine that this curvature–pressure evolution might find application as a passive soft robotic gripper, with the unusual feature that the unpressurized device is clenched (i.e. curved), whilst the pressurized device is open (i.e. flat) [48,49].

To demonstrate this novel route for the control of curvature, we consider experiments with a four cell structure based on our design with an asymmetry in the clamping angles between the top and bottom surface walls; this structure is 3D-printed in Agilus-30 and inflated using a syringe while lying horizontally on a surface (see figure 8). The pressure is measured using a digital manometer (RS PRO RS-8890, Radio Spares, UK). The modulus of Agilus-30 is known to be highly sensitive to temperature so experiments were performed in environments with different ambient temperatures in the range 19°C–24°C; this temperature was measured using an infrared thermometer and the corresponding Young's modulus was inferred from separate experiments in a tensile tester (Yunlan Zhang 2022, private communication). The effective curvature of the device at different pressures was inferred by measurements from images of the inflation.

Experimental measurements of the effective curvature at different air pressures are compared with the predictions of the two-dimensional model in figure 8f. These results confirm that the effective curvature of the device decreases with increased pressure, as expected, though the magnitude of the decrease is larger than expected at the measured pressures. This agreement is rather satisfactory given the variability in modulus according to print runs and the three-dimensional nature of the experimental set-up that differs from our simplified, two-dimensional model. Our analytical framework may thus provide a starting point and/or an alternative to more intricate numerical techniques, such as finite element simulations, which are often used to model such systems.

6. Discussion and conclusions

In this paper, we have presented a simple model through which the turgor-induced mechanics of monolayer cellular sheets can be understood. We began by seeking to understand whether the familiar influence of turgor on the ability of plant leaves to resist the effects of gravity applies also to structures that are a single cell thick and do not have vasculature. We developed a

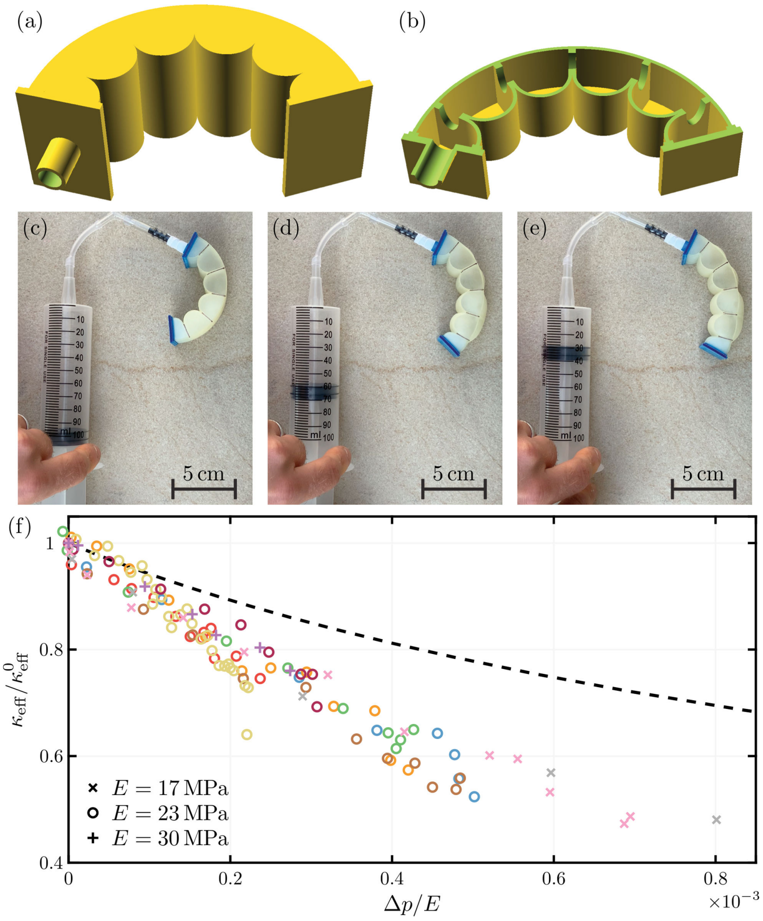

Figure 8. A 3D-printed realization of the asymmetric pressurized structure of figure 4 uncurves upon pressurization. Panel (*a*) shows a three-dimensional render of the full computer aided design (CAD), while panel (*b*) shows a half section. To enable inflation, the device has been designed with a 'lid' and a 'base' in the third-dimension (separated by 30 mm). The other geometrical parameters are $L_{\text{L}} = 10$ mm, $L_{\pm} = 20$ mm, $h_{\text{L}} = 1$ mm, $h_{\pm} = 1$ mm, $\theta_+ = 0$ and $\theta_- = \pi/2$. Equal pressurization of each cell is ensured by elliptical holes (of width 6 mm and length 12 mm) that connect neighbouring cells—as seen in (*b*). The structure was 3D printed using the PolyJet elastomer Agilus-30 [50]. Panels (*c*)–(*e*) show increasing pressurizations ($\Delta p = 0$, 5.87 kPa and 8.13 kPa, respectively) of the 3D-printed structure with the effective curvature, κ_{eff}, decreasing correspondingly. Quantitative measures of the macroscopic curvature as a function of measured air pressure are presented in the main figure of (*f*); different colours indicate different experimental runs and different shapes indicate different Young's modulus, E, as given in the key. The predicted effective curvature from the two-dimensional model developed here is plotted as the black dashed curve.

simple model of a two-dimensional monolayer to determine the resistance to bending that might be expected to emerge from the turgor-induced elastic deflection of the cell walls. (This two-dimensional model is expected to provide a lower bound on the resistance to bending of such structures since curvature in the neglected third dimension is expected to give a geometry-induced rigidity [51]). This allowed us to consider scenarios in which the cells have sharp corners, as is suggested by cross-sections of moss leaves (see figure 1a), but which are difficult to describe using shell theory, for example. Our model was able to quantitatively reproduce previous observations of turgor-induced shrinkage in cell monolayers Hofhuis *et al*. [30], and shows that most moss leaves are small enough that the enhancement of their rigidity by turgor is relatively small.

Given the relative unimportance of turgor pressure for providing mechanical support against gravity in moss leaves, we also considered the curling/uncurling that is observed as water content decreases/increases. In particular, we investigated the effect of different asymmetries in the cellular structure on the curling that results from a decrease in pressure (corresponding to desiccation), focusing on two types of asymmetries: mechanical (e.g. asymmetries in the elastic moduli) and geometrical (e.g. asymmetries in wall lengths/angles). We found that mechanical asymmetries only lead to curvature in turgid conditions, with the structure remaining symmetric when flaccid. Conversely, we found that geometrical asymmetries lead to a natural curvature in flaccid conditions, but that this curvature is ironed out in turgid conditions. Since this is in keeping with observations of moss leaves (which we demonstrated in the context of *Physcomitrium patens* moss leaves in figure 7), we conclude that the underlying cause of the leaf-curling observed biologically is likely to be a geometrical, rather than mechanical, asymmetry. However, we emphasize that our model did not account for variations of the underlying physical properties, and their anisotropy, with water content—an effect that is well known in paper, for example [52,53].

Finally, we illustrated the importance, and potential utility, of introducing a cell-level asymmetry in inflatable structures by presenting a pneumatically inflated structure whose curvature mimics that of moss leaves as the internal pressure changes: at low pressure (flaccid) the structure is curved, while at high pressure (turgid) the structure flattens out. Such a structure may have applications in soft robotics where it might represent a gripper in which internal pressurization is only required to release an object, rather than to keep hold of it. This would reduce the risk of damage induced by over-pressurization [54], and would provide yet another example for plant-inspired soft robotics [10,55]. We note that extending this model system to multi-cell structures may provide additional insights into more complicated, non-vascular, plant structures or alternative mechanisms for the strain-dependent properties of certain plant tissues [56]. However, such extensions of our model may require the inclusion of three-dimensional effects.

Ethics. This work did not require ethical approval from a human subject or animal welfare committee.

Data accessibility. The data associated with our paper is now publicly accessible at [25].

Supplementary material is available online [24].

Declaration of AI use. We have not used AI-assisted technologies in creating this article.

Authors' contributions. T.G.J.C.: formal analysis, methodology, writing—original draft; J.F.: investigation, visualization; O.S.: methodology; J.-M.A.: resources, writing—review and editing; P.M.: investigation, methodology, resources; A.B.: conceptualization, methodology, supervision, writing—original draft, writing—review and editing; D.V.: conceptualization, formal analysis, investigation, methodology, supervision, writing—original draft.

All authors gave final approval for publication and agreed to be held accountable for the work performed therein.

Conflict of interest declaration. We declare we have no competing interests.

Funding. The research leading to these results has received funding from the Leverhulme Trust (D.V.), the EPSRC Programme Grant 'From Sensing to Collaboration' EP/V000748/1 (P.M.), and Agence Nationale de la Recherche, GrowFlat, ANR-21-CE30-0039-01 (A.B.).

Acknowledgements. We are grateful to Yunlan Zhang for sharing her data on the modulus of Agilus-30 at different ambient temperature; Yoan Coudert for providing *Physcomitrium patens*; and Madeleine Seale for imaging trials.

Appendix A. Independence of infinitesimal bending modulus on pressure

Given the everyday observation that pressure is integral to the rigidity of structures from plant leaves to cylindrical balloons, the claim that the resistance to bending at small curvatures is independent of pressure is surprising and generally involves a detailed calculation [12,13]. For a more intuitive feeling, consider bending a pressurized two-dimensional section through a pressurized shell, as sketched in figure 9. Here, the two-dimensional section consists of two surface walls (of thickness h and Young's modulus E) held parallel to each other with a vertical separation t. Pressurizing the interior induces a tension (thickness-integrated stress), T_p, in the two walls; for instance, for a cylindrical balloon of radius R, we would expect $T_p = pR/2$. Bending the section downwards to form a midline curvature, κ, induces a differential strain across the section, which stretches the top surface wall and compresses the bottom surface wall by a strain $\varepsilon = t\kappa/2$. Assuming Hooke's law, the tension in the top and bottom surface walls then becomes $T = T_p \pm Eht\kappa/2$, respectively. Notably, the moment (about the midline) required to impose such a deformation, $\mu = Eht^2\kappa/2$, corresponds to $B_{\mathrm{eff}} = Eht^2/2$. This B_{eff} is independent of T_p and, hence, the internal pressure, p.

Appendix B. Further size limits for monolayer leaves

In §4.2, we introduced the elastogravitational length, ℓ_{bg}, of the cellular structure. We showed that ℓ_{bg} increases with the turgor pressure, p, in monolayer moss leaves and, for certain species, turgor is required for the leaf deflection, $\mathcal{D} \approx \ell^3/(2\ell_{\mathrm{bg}})^3$, to be sufficiently small that the leaf supports itself under gravity. An alternative constraint on leaf growth might be the requirement that the differential strain caused by bending ($\mathcal{E} = \ell_{\mathrm{thick}}\kappa/2$, where κ is the curvature of the leaf and ℓ_{thick} is its macroscopic thickness) is small.

To estimate the curvature, κ, and, hence, the strain, $\mathcal{E}$, we use the small deflection profile of a Euler–Bernoulli beam, i.e.

$$w(x) = \frac{1}{24\ell_{\mathrm{bg}}^3} x^2\left(6\ell^2 - 4\ell x + x^2\right), \tag{B 1}$$

where $0 \le x \le \ell$ [26]. This solution was used to estimate the deflection in (4.1), i.e. $\mathcal{D} := w(\ell)/\ell$, and also provides an estimate of the strain,

$$\mathcal{E} := \frac{\ell_{\mathrm{thick}}}{2} w''(\ell) = \frac{\ell_{\mathrm{thick}}\ell^2}{4\ell_{\mathrm{bg}}^3}. \tag{B 2}$$

Thus, for the strain induced by bending to be sufficiently small, we require $\ell/2$ to be small in comparison with $\ell_{\mathrm{bend}} := (\ell_{\mathrm{bg}}^3/\ell_{\mathrm{thick}})^{1/2} = [B_{\mathrm{eff}}/(\rho g \ell_{\mathrm{thick}}^2)]^{1/2}$.

In figure 10, the leaf widths, ℓ_{width}, of nine different species of single-cell thick moss leaves are plotted against the corresponding bending lengths, $\ell_{\mathrm{bend}} = [B_{\mathrm{eff}}/(\rho g \ell_{\mathrm{thick}}^2)]^{1/2}$, predicted from our model. Here, we use the same data as that used in figure 6. By comparing figure 10a, for a flaccid cell, and figure 10b, for a turgid cell, it is apparent that the turgor pressure increases the bending length, ℓ_{bend}. In fact, using the small deflection solution, (B 2) with $\ell = \ell_{\mathrm{width}}/2$, the expected bending-induced strains of the turgid leaves are less than 0.1%, i.e. $[(\ell_{\mathrm{width}}/2)/\ell_{\mathrm{bend}}]^2 = 4 \times \mathcal{E} < 4 \times 10^{-3}$. However, this is not true when $p = 0$ for certain species (as was the case for the elastogravitational length in figure 6).

Overall, figures 6 and 10 provide safety factors for the surface extension of moss leaves. An additional size limit of monolayer structures is that ℓ must be much smaller than the length scale over which the effective beam stretches due to gravity, i.e. $\ell_{\mathrm{stretch}} := Y_{\mathrm{eff}}/(\rho g \ell_{\mathrm{thick}})$, where Y_{eff} is the effective stretching modulus introduced in section II.B of [25]. However, for the moss species considered here, ℓ_{stretch} is orders of magnitude larger than ℓ_{bg} and ℓ_{bend}, thus it does not provide a principal constraint on the surface extension of moss leaves.

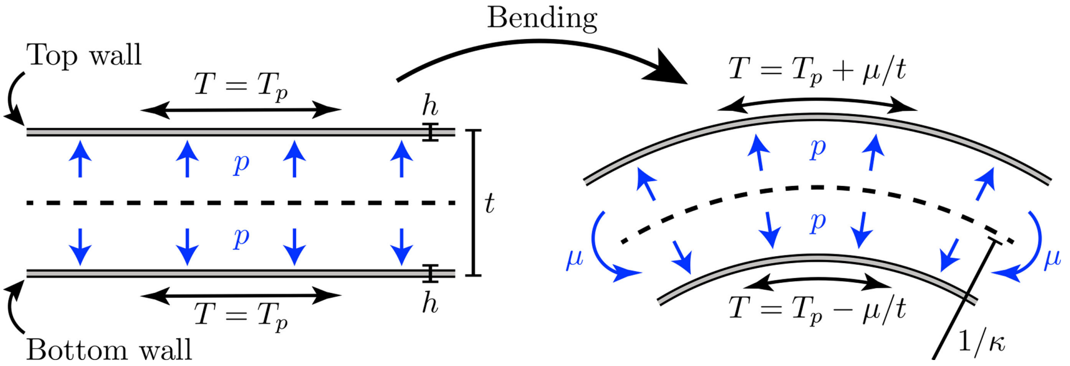

Figure 9. Sketch of the bending of a pressurized two-dimensional channel. In the left sketch, an interior pressure, p, induces a tension, T_p, in the two bounding surface walls. In the right sketch, the pressurized channel is bent under a moment, μ, which induces a differential strain across the channel.

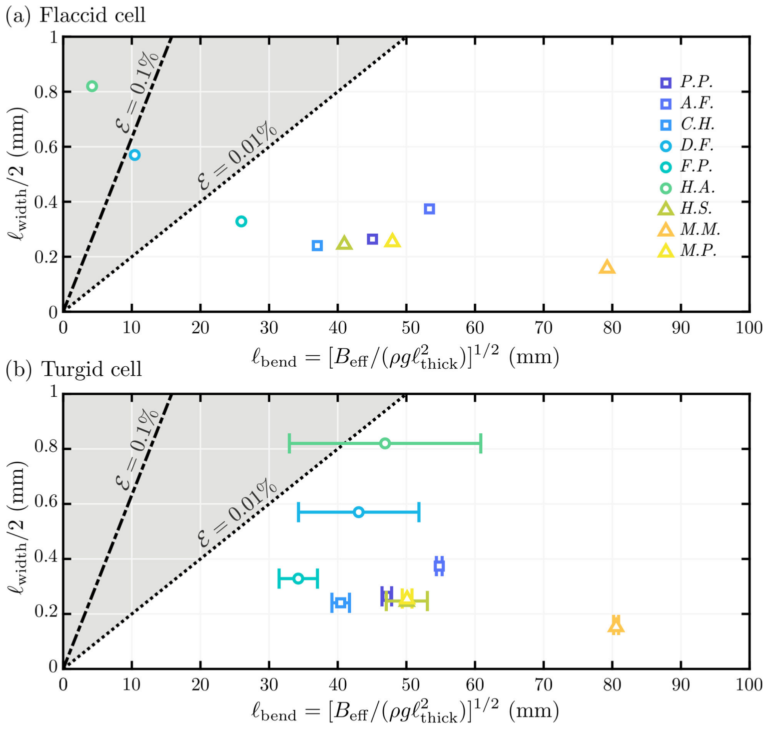

Figure 10. Plot of the extended lamina widths, $\ell_{\mathrm{width}}/2$, against estimated strain length, $\ell_{\mathrm{bend}} = [B_{\mathrm{eff}}/(\rho g \ell_{\mathrm{thick}}^2)]^{1/2}$, for nine species of single-cell thick moss, defined by colour, and point shape denoting the type: trunk-dwelling mosses, □, (*Pyrrhobryum pungens*, *Acroporium fuscoflavum*, *Campylopus hawaiicus*); ground-dwelling mosses, ◯, (*Distichophyllum freycinetii*, *Fissidens pacificus*, *Hookeria acutifolia*); branch-dwelling mosses, △, (*Holomitrium seticalycinum*, *Macromitrium microstomum*, *Macromitrium piliferum*). Here, we have used the cell width, cell height, interior and surface cell wall thicknesses, lamina thickness and maximum leaf width from [21] to estimate L, L_{L}, h_{L}, h_{S}, ℓ_{thick} and ℓ_{width}, respectively. We further assume a density $\rho = 1000\ \mathrm{kg\ m^{-3}}$; clamping angle $\Theta = \pi/4$ (an approximation based on cell photographs [21]); Young's moduli $E_{\mathrm{L}} = E_{\mathrm{S}} = 100$ MPa, which are chosen as a lower bound to the typically accepted range in plant cells [45]; and turgor pressures (a) $p = 0$ MPa (i.e. a flaccid cell) and (b) $0.8\ \mathrm{MPa} \leq p \leq 2.1$ MPa (the typical range found in moss [33], which gives the range in ℓ_{bend}). The lines $\ell_{\mathrm{width}}/2 = 2\mathcal{E}^{1/2}\ell_{\mathrm{bend}}$ for $\mathcal{E} = 10^{-3}$ (dash-dotted) and $\mathcal{E} = 10^{-4}$ (dotted), correspond to the maximal differential strain, $\mathcal{E}$, caused by bending a Euler–Bernoulli beam, and the shaded region corresponding to significant deformations under gravity.

Appendix C. Experiments with *Physcomitrium patens*

Physcomitrium patens (Gransden strain) was grown on medium (0.2%, Gamborg's B5 media with vitamins, Duchefa) mixed with agar (1.2% plant agar, Duchefa), a phytotron (Aralab) with 24 h lighting (≈ 5300 lx) at 22°C. *Physcomitrium* leaves were observed fresh and kept on a wet glass slide (enough water to moisturize the sample without drowning it) and then dried upon a 37°C heating plate for about 14 min. Wet and dry leaves were imaged with an optical coherence tomography system (Ganymede-SP5, Thorlabs) using an objective (LMS02-BB) with a 5 × 5 mm field of view and a pixel size of 10 × 10 × 1.95 µm (the smallest size is vertical). The ThorImage software (Thorlabs) was used for TIFF file extraction. TIFF stacks were processed with ImageJ for the extraction of curvature. Example cross-sections of a dehydrated and hydrated *Physcomitrium patens* leaf are shown in figure 7 in the main text.

References

1. Kwan KW, Ye ZW, Chye ML, Ngan AHW. 2013 A mathematical model on water redistribution mechanism of the seismonastic movement of *Mimosa pudica*. *Biophys. J.* **105**, 266–275. (doi:10.1016/j.bpj.2013.06.001)
2. Sleboda DA, Geitmann A, Sharif-Naeini R. 2023 Multiscale structural anisotropy steers plant organ actuation. *Curr. Biol*. **33**, 639–646.(doi:10.1016/j.cub.2022.12.013)
3. Mader A, Langer M, Knippers J, Speck O. 2020 Learning from plant movements triggered by bulliform cells: the biomimetic cellular actuator. *J. R. Soc. Interface* **17**, 20200358. (doi:10.1098/rsif.2020.0358)
4. Louf JF, Guéna G, Badel E, Forterre Y. 2017 Universal poroelastic mechanism for hydraulic signals in biomimetic and natural branches. *Proc. Natl Acad. Sci*. USA **114**, 11034–11039. (doi:10.1073/pnas.1707675114)
5. Dumais J, Forterre Y. 2012 "Vegetable dynamicks": the role of water in plant movements. *Annu. Rev. Fluid Mech*. **44**, 453–478. (doi:10.1146/annurev-fluid-120710-101200)
6. Scoffoni C, Vuong C, Diep S, Cochard H, Sack L. 2014 Leaf shrinkage with dehydration: coordination with hydraulic vulnerability and drought tolerance. *Plant Physiol*. **164**, 1772–1788. (doi:10.1104/pp.113.221424)
7. Glime JM. 2017 *Bryophyte ecology*. Michigan Technological University and the International Association of Bryologists. See https://digitalcommons.mtu.edu/bryophyte-ecology/.
8. Rafsanjani A, Brulé V, Western TL, Pasini D. 2015 Hydro-responsive curling of the resurrection plant *Selaginella lepidophylla*. *Sci. Rep*. **5**, 8064. (doi:10.1038/srep08064)
9. Balachandran A, Ravindran NA, Mohd G, Bhat IM, Priyadarshini S, Lone S. 2024 Bioinspired moisture-driven soft robotic actuator. *Adv. Intell. Syst*. 00609. (doi:10.1002/aisy.202400609)
10. Guo K, Liu M, Vella D, Suresh S, Hsia KJ. 2024 Dehydration-induced corrugated folding in *Rhapis excelsa* plant leaves. *Proc. Natl Acad. Sci*. USA **121**, e2320259121. (doi:10.1073/pnas.2320259121)
11. Roberts AW, Roberts EM, Haigler CH. 2012 Moss cell walls: structure and biosynthesis. *Front. Plant Sci*. **3**, 166. (doi:10.3389/fpls.2012.00166)
12. Haseganu EM, Steigmann DJ. 1994 Theoretical flexural response of a pressurized cylindrical membrane. *Int. J. Solids Struct*. **31**, 27–50. (doi:10.1016/0020-7683(94)90173-2)
13. Qiu L, Hutchinson JW, Amir A. 2022 Bending instability of rod-shaped bacteria. *Phys. Rev. Lett*. **128**, 058101. (doi:10.1103/physrevlett.128.058101)
14. Siéfert E. 2019 Inflating to shape: from soft architectured elastomers to patterned fabric sheets. PhD thesis, Sorbonne Université, Paris, France.
15. Siéfert E, Reyssat E, Bico J, Roman B. 2019 Programming curvilinear paths of flat inflatables. *Proc. Natl Acad. Sci*. USA **116**, 16692–16696. (doi:10.1073/pnas.1904544116)
16. Gao T, Bico J, Roman B. 2023 Pneumatic cells toward absolute Gaussian morphing. *Science* **381**, 862–867. (doi:10.1126/science.adi2997)
17. Barton B. 2016 Recent work on the design and construction of air inflated structures. *Procedia Eng*. **155**, 47–60. (doi:10.1016/j.proeng.2016.08.006)
18. Sinibaldi E, Puleo GL, Mattioli F, Mattoli V, Di Michele F, Beccai L, Tramacere F, Mancuso S, Mazzolai B. 2013 Osmotic actuation modelling for innovative biorobotic solutions inspired by the plant kingdom. *Bioinspir. Biomim*. **8**, 025002. (doi:10.1088/1748-3182/8/2/025002)
19. Sinibaldi E, Argiolas A, Puleo GL, Mazzolai B. 2014 Another lesson from plants: the forward osmosis-based actuator. *PLoS One* **9**, e102461. (doi:10.1371/journal.pone.0102461)
20. Waite M, Sack L. 2010 How does moss photosynthesis relate to leaf and canopy structure? Trait relationships for 10 Hawaiian species of contrasting light habitats. *New Phytol*. **185**, 156–172. (doi:10.1111/j.1469-8137.2009.03061.x)
21. Charron AJ, Quatrano RS. 2009 Between a rock and a dry place: the water-stressed moss. *Mol. Plant* **2**, 478–486. (doi:10.1093/mp/ssp018)
22. Hu R, Xiao L, Bao F, Li X, He Y. 2016 Dehydration-responsive features of *Atrichum undulatum*. *J. Plant Res*. **129**, 945–954. (doi:10.1007/s10265-016-0836-x)
23. Vella D. 2019 Buffering by buckling as a route for elastic deformation. *Nat. Rev. Phys*. **1**, 425–436. (doi:10.1038/s42254-019-0063-1)
24. Chandler TGJ, Ferria J, Shorthose O, Allain JM, Maiolino P, Boudaoud A *et al*. 2025 Supplementary material from: Mechanics of pressurized cellular sheets. Figshare. (doi:10.6084/m9.figshare.c.7658831)
25. Chandler T, Vella D. 2024 *Data for mechanics of pressurized cellular sheets*. Oxford, UK: University of Oxford. (doi:10.5287/ora-brdm8y2ez)
26. Howell P, Kozyreff G, Ockendon J. 2008 Applied solid mechanics. Cambridge, UK: Cambridge University Press.
27. O'Reilly OM. 2017 Applications of the Mechanics of a String. In *Modeling nonlinear problems in the mechanics of strings and rods*, pp. 49–92. New York, NY: Springer International Publishing. (Interaction of Mechanics and Mathematics). (doi:10.1007/978-3-319-50598-5_2)
28. Pandey A, Moulton DE, Vella D, Holmes DP. 2014 Dynamics of snapping beams and jumping poppers. *EPL* **105**, 24001. (doi:10.1209/0295-5075/105/24001)
29. Marthelot J, Brun PT, Jiménez FL, Reis PM. 2017 Reversible patterning of spherical shells through constrained buckling. *Phys. Rev. Mater*. **1**, 025601. (doi:10.1103/physrevmaterials.1.025601)
30. Hofhuis H *et al*. 2016 Morphomechanical innovation drives explosive seed dispersal. *Cell* **166**, 222–233. (doi:10.1016/j.cell.2016.05.002)
31. Plummer A, Nelson DR. 2020 Buckling and metastability in membranes with dilation arrays. *Phys. Rev. E* **102**, 033002. (doi:10.1103/physreve.102.033002)
32. Proctor MCF, Ligrone R, Duckett JG, Proctor MCF, Ligrone R, Duckett JG. 2007 Desiccation tolerance in the moss *Polytrichum formosum*: physiological and fine-structural changes during desiccation and recovery. *Ann. Bot*. **99**, 75. (doi:10.1093/aob/mcm098)
33. Wang Q, Giudici A, Huang W, Wang Y, Liu M, Tawfick S, Vella D. 2024 Transient amplification of broken symmetry in elastic snap-through. *Phys. Rev. Lett*. **132**, 267201. (doi:10.1103/physrevlett.132.267201)
34. Kierzkowski D, Nakayama N, Routier-Kierzkowska AL, Weber A, Bayer E, Schorderet M, Reinhardt D, Kuhlemeier C, Smith RS. 2012 Elastic domains regulate growth and organogenesis in the plant shoot apical meristem. *Science* **335**, 1096–1099. (doi:10.1126/science.1213100)
35. Hadjaje S, Andrade-Silva I, Dalbe MJ, Clément R, Marthelot J. 2024 Wings expansion in *Drosophila melanogaster*. *Nat. Commun* **15**, 10577. (doi:10.1038/s41467-024-54527-0)
36. Siéfert E, Reyssat E, Bico J, Roman B. 2020 Programming stiff inflatable shells from planar patterned fabrics. *Soft Matter* **16**, 7898–7903. (doi:10.1039/d0sm01041c)
37. Wang CY. 1986 A critical review of the heavy elastica. *Int. J. Mech. Sci*. **28**, 549–559. (doi:10.1016/0020-7403(86)90052-4)
38. Holmes DP. 2019 Elasticity and stability of shape-shifting structures. *Curr. Opin. Colloid Interface Sci*. **40**, 118–137. (doi:10.1016/j.cocis.2019.02.008)
39. Wei Z, Mandre S, Mahadevan L. 2012 The branch with the furthest reach. *EPL* **97**, 14005. (doi:10.1209/0295-5075/97/14005)
40. Tadrist L, Darbois-Texier B. 2016 Are leaves optimally designed for self-support? An investigation on giant monocots. *J. Theor. Biol*. **396**, 125–131. (doi:10.1016/j.jtbi.2016.02.018)
41. Cosgrove DJ. 2016 Plant cell wall extensibility: connecting plant cell growth with cell wall structure, mechanics, and the action of wall-modifying enzymes. *J. Exp. Bot*. **67**, 463–476. (doi:10.1093/jxb/erv511)
42. Niklas KJ, Paolillo DJ Jr. 1997 The role of the epidermis as a stiffening agent in *Tulipa* (Liliaceae) stems. *Am. J. Bot*. **84**, 735–744. (doi:10.2307/2445809)
43. Fouchard J, Wyatt TPJ, Proag A, Lisica A, Khalilgharibi N, Recho P, Suzanne M, Kabla A, Charras G. 2020 Curling of epithelial monolayers reveals coupling between active bending and tissue tension. *Proc. Natl Acad. Sci*. USA **117**, 9377–9383. (doi:10.1073/pnas.1917838117)
44. Hofmeister W. 1859 Über die Beugungen saftreicher Pflanzenteile nach Erschütterung. *Jb. Wiss. Bot* **2**, 237–266.

45. Cadogan D, Smith T, Uhelsky F, Mackusick M. 2004 Morphing inflatable wing development for compact package unmanned aerial vehicles. *45th AIAA/ASME/ASCE/AHS/ASC Structures, Structural Dynamics & Materials Conf*. American Institute of Aeronautics and Astronautics. (doi:10.2514/6.2004-1807)

46. Jones TJ, Jambon-Puillet E, Marthelot J, Brun PT. 2021 Bubble casting soft robotics. *Nature* **599**, 229–233. (doi:10.1038/s41586-021-04029-6)

47. Chen T, Yang X, Zhang B, Li J, Pan J, Wang Y. 2024 Scale-inspired programmable robotic structures with concurrent shape morphing and stiffness variation. *Sci. Robot*. **9**, eadl0307. (doi:10.1126/scirobotics.adl0307)

48. Ilievski F, Mazzeo AD, Shepherd RF, Chen X, Whitesides GM. 2011 Titelbild: soft robotics for chemists (Angew. Chem. 8/2011). *Angew. Chem. Weinheim Bergstr. Ger*. **123**, 1765. (doi:10.1002/ange.201000255)

49. Rus D, Tolley MT. 2015 Design, fabrication and control of soft robots. *Nature* **521**, 467–475. (doi:10.1038/nature14543)

50. Abayazid FF, Ghajari M. 2020 Material characterisation of additively manufactured elastomers at different strain rates and build orientations. *Addit. Manuf*. **33**, 101160. (doi:10.1016/j.addma.2020.101160)

51. Taffetani M, Box F, Neveu A, Vella D. 2019 Limitations of curvature-induced rigidity: how a curved strip buckles under gravity. *EPL* **127**, 14001. (doi:10.1209/0295-5075/127/14001)

52. Reyssat E, Mahadevan L. 2011 How wet paper curls. *EPL* **93**, 54001. (doi:10.1209/0295-5075/93/54001)

53. Bosco E, Peerlings RHJ, Geers MGD. 2015 Predicting hygro-elastic properties of paper sheets based on an idealized model of the underlying fibrous network. *Int. J. Solids Struct*. **56–57**, 43–52. (doi:10.1016/j.ijsolstr.2014.12.006)

54. Pontin M, Damian DD. 2024 Multimodal soft valve enables physical responsiveness for preemptive resilience of soft robots. *Sci. Robot*. **9**, eadk9978. (doi:10.1126/scirobotics.adk9978)

55. Must I, Sinibaldi E, Mazzolai B. 2019 A variable-stiffness tendril-like soft robot based on reversible osmotic actuation. *Nat. Commun* **10**, 344. (doi:10.1038/s41467-018-08173-y)

56. Lipchinsky A, Sharova EI, Medvedev SS. 2013 Elastic properties of the growth-controlling outer cell walls of maize coleoptile epidermis. *Acta Physiol. Plant*. **35**, 2183–2191. (doi:10.1007/s11738-013-1255-4)